IEEE Robotics and Automation Letters (RA-L) paper, presented at ICRA 2026, Vienna, Austria. Cite as RA-L paper.

Continuum Robot Segments with High Output Stiffness via Diagonal Backbones

Ethan Eisenhauer[1], *Student Member, IEEE*, Eli Milam[1], Joshua Gaston[1], and Caleb Rucker[1], *Senior Member, IEEE*

***Abstract*—Continuum robots offer unique advantages for applications such as minimally invasive surgery, navigation through confined environments, and safe human-robot interaction. However, while most continuum robot segments are designed to exhibit constant curvature over their length, they passively deform into a non-constant curvature s-shape when holding payloads at the tip, and their dynamic movement is often subject to unwanted vibration of the passive non-constant curvature modes. In this paper, we propose a simple solution to dramatically improve these issues: a continuum robot segment design that utilizes a diagonal backbone and flexible push-pull actuation rods. This simple modification to common continuum-robot construction enables us to eliminate the passive s-shaped mode, creating a bending segment that can handle large loads without significant deformation or vibration while requiring no more actuation force than conventional designs. We show that a modified version of 1-DOF constant-curvature kinematics accurately describes the structure when actuator translations are equal and opposite. We also develop and validate a 2-DOF model that predicts tip position and orientation resulting from more general actuation inputs. The models and increased output stiffness were verified experimentally and the concept was demonstrated on a multi-segment robot following a 3D trajectory with minimal disturbance from added loads.**

***Index Terms*—Soft Robot Materials and Design; Modeling, Control, and Learning for Soft Robots; Flexible Robotics; Tendon/Wire Mechanism**

I. Introduction

CONTINUUM robots are defined by a continuous structure with infinite kinematic degrees of freedom [1]. They provide unique advantages in shape flexibility and can be manufactured at smaller scales than rigid-link robots, making them advantageous for applications in confined spaces such as minimally invasive surgery [2]–[4], inspection operations [5]–[7], and for human-robot interaction [8], [9].

A main limitation of continuum robots in some applications is that their flexibility entails low output stiffness at the tip of the robot. A large tip load will usually cause large tip deflection, which limits the force a continuum robot can apply and the weight that it can carry. Even when not carrying large tip loads, the low output stiffness results in undesired tip vibrations when executing fast motions, making it difficult to precisely control tip location.

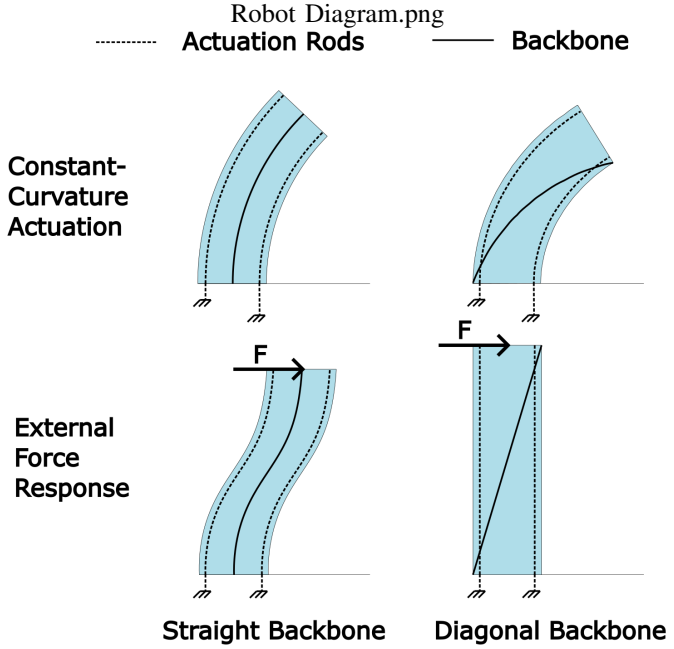

Fig. 1: This figure shows how both a straight-backbone continuum robot and a diagonal backbone continuum robot respond to constant curvature actuation and external loads. Both robot designs have a similar response to constant curvature actuation, although the diagonal-backbone is asymmetrical as compared to the straight-backbone continuum robot. Under external load, the straight-backbone continuum robot deforms into the S-shape. The diagonal backbone robot does not deform.

Many approaches have been taken to selectively increase continuum robot stiffness while maintaining range of motion. This includes jamming approaches [10]–[13] pneumatic stiffening of joints in [14]–[16], rod-based locking [17], and topology optimization in [18]. These efforts are primarily designed to increase stiffness in general (or at a specific time) and come with the tradeoffs of increased force required to move the robot while it is stiff and often reduced range of motion.

A primary reason many continuum robots have low output stiffness is the existence of passive modes of deformation. One usually passive mode is torsion, which can be significant when the robot is under external loads. Torsion can be mitigated and strength improved by hybrid rigid-continuum structures [19], origami-inspired structural designs such as those using

Manuscript received: April, 30, 2025; Revised July, 27 2025; Accepted October, 15, 2025.

This paper was recommended for publication by Cecilia Laschi upon evaluation of the Associate Editor and Reviewers' comments.

This work was supported in part by NSF under EFMA-1935278 and in part by NIH under R01-EB032385. The views reflected in this paper are those of the authors and not necessarily endorsed by the NSF or NIH.

[1]University of Tennessee, Department of Mechanical and Aerospace Engineering

Digital Object Identifier (DOI): see top of this page.

IEEE Robotics and Automation Letters (RA-L) paper, presented at ICRA 2026, Vienna, Austria. Cite as RA-L paper.

a Yoshimura fold pattern [20], [21] or accordion folds [22], and torsion can be actively controlled through the use of Kresling patterns [23], [24]. In addition to torsion, most continuum robots have modes in which the robot can bend without changing the length of any of its actuation lines (i.e. the physical paths along which actuation tendons or rods are routed). Thus, even when actuators are locked and the lines stay constant length, the segment can deform (into an s-shape, as illustrated in Figure 1), and the tip can deflect. This fact has been recognized in prior papers, and strategies to address it have been proposed. In [25], the authors observe the s-shape passive mode and mitigate it with a variable neutral line mechanism based on rolling contact joints with a specific shape. In [26] and [27] a chain of synchronized linkages enforces constant curvature in a pseudo-continuum device. In [28], it was shown that convergent tendon routing paths dramatically increase the output stiffness due to the elimination of the s-shape mode. This approach was carried further in [22] by using a combination of six non-parallel push-pull actuation rods in an origami-inspired compressible structure to achieve high output stiffness in all directions. The tradeoff with the strategies in [28] (Oliver-Butler et al.) and [22] (Childs and Rucker) is that non-parallel actuation lines create complications in robot design, construction, and modeling. Constant curvature kinematics no longer applies, and the actuation lines must be creatively routed back through curved transmission paths to the stationary actuator pack. (for example, see Figures 7 and 8 in [22]).

In this paper we address these limitations by presenting and studying a simple planar continuum robot segment design using a flexible diagonal backbone and conventional straight actuation lines. This approach inherits the dramatic increase in output stiffness associated with convergent actuator routing as explored in [22], [28] by leveraging geometry, but reduces complexity because the actuation lines remain parallel to the longitudinal axis of the segment and do not require complicated routing schemes. We further verify that this design still exhibits constant curvature along the diagonal backbone when the two actuation lines are actuated an equal amount in opposite directions. We provide a kinematic model for this simple case, and also extend the model to consider general actuation that leads to a 2-DOF planar segment workspace. We further construct a single-segment prototype, experimentally validate the accuracy of our two models, validate the dramatic increase in output stiffness, and demonstrate the concept of a multi-segment robot by building and testing a two-segment prototype.

II. Design

Our proposed bending segment structure is formed by two plates, one at the base and one at the tip, connected diagonally by a backbone, as shown in Figure 2. Triangular fins are added to the backbone to increase the torsional stiffness while maintaining low bending stiffness in the primary bending direction [29]. The triangular fins swap sides halfway down the backbone to use the space well, and straight fins are extended across the backbone on the other side. Actuation

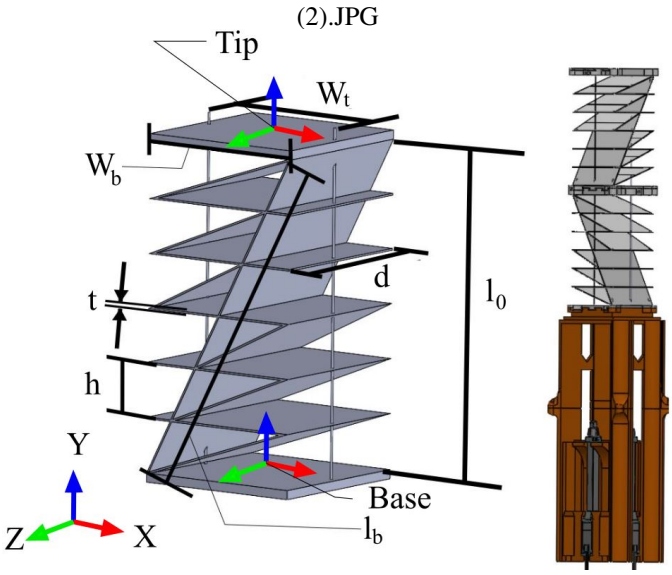

Fig. 2: The left image defines the dimensions of a segment. w_b is the width of the base, and w_t is the distance between actuation rods. d is the depth. t is the thickness. l_0 is the height between fins. l_b is the length of the backbone. The right image shows the CAD model for the two segment assembly where two segments are combined at a 90 degree offset to create a 4-DOF robot.

rods are routed parallel to the y-axis of the segment with guide-holes through the fins, represented by the dotted lines. The rods are attached to the tip plate on one end and linear actuators on the other (below the base), using set screws. The segment is actuated by extending or contracting the rods, which results in the elongation or compression along the sides of the segment. Conventional planar bending segments with a straight backbone exhibit only 1 DOF (constant curvature bending) even with two push-pull actuation rods, while the diagonal backbone segment allows control of 2-DOF motion in the plane, while still being able to produce the conventional constant-curvature configuration, as we demonstrate later in the paper.

We constructed prototype bending segments for validation experiments discussed later in the paper. The prototype segments uses a backbone thickness of t = 0.8 mm, width of w_b = 75 mm, a rod width of w_t = 67 mm, a depth of d = 75 mm, an inner segment length of l_0 = 144 mm which is the distance between the interior faces of the plates, a backbone length of l_b = $\sqrt{l_o^2 + w_b^2}$, and a pitch height of h = 24 mm, shown in Figure 2 (left). The width and depth were chosen to allow room for a simple actuation strategy using four linear stepper actuator directly in line with the rods as shown in Figure 2 (right). The other dimensions (length and triangle shape) were chosen to increase the effectiveness of the triangular fins, increasing the torsional stiffness and bending stiffness about the x-axis, while allowing for bending about the y-axis.

The segment was fabricated using 3D printed PETG from a Bambu X1 carbon printer. The segment can be printed flat as a single piece with no post-processing. The single segment design was actuated by two Actuonix S20 100mm linear stepper motors. The motors are housed in the base of the structure, underneath all of the arm segments. A puzzle

IEEE Robotics and Automation Letters (RA-L) paper, presented at ICRA 2026, Vienna, Austria. Cite as RA-L paper.

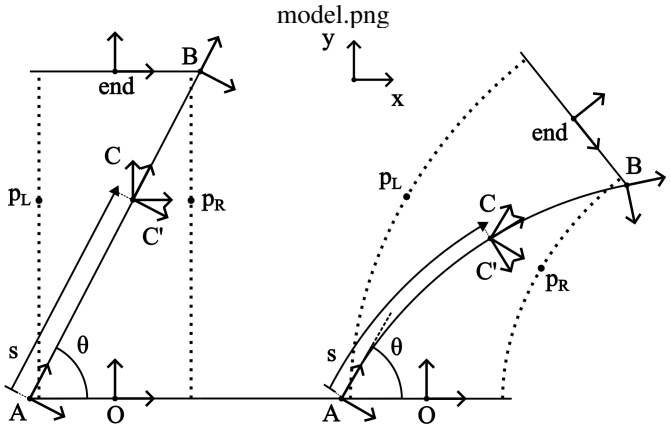

Fig. 3: This diagram outlines all frames and geometric parameters used for both kinematic models. O is the origin frame defined at the base of the segment. end is the end effector frame of the segment defined at the segment tip. A, B, C' and C are intermediate frames used to represent end, $\mathbf{p}_R$, and $\mathbf{p}_L$ in the O frame. $\mathbf{p}_R$ and $\mathbf{p}_L$ are points on the right and left actuation rods that are also constrained horizontal to C. θ is the angle of the backbone relative to the base, which remains constant even under bending. s is the distance along the backbone from the base to some point.

piece interlock was used to join the plates rigidly at the base of the segments.

III. Modeling: 1-DOF Constant Curvature along a Diagonal Backbone

In this section, we derive a kinematic model based on the assumption of constant curvature along the diagonal backbone. While this model uses conventional robotics methods (constant-curvature transformations, basic reference frame assignment) it provides different predictions than a the widely used constant curvature segment model reviewed in [1], because it contains a pre- and post- transformation to account for the fact that the backbone is diagonal instead of parallel to the actuation rods. Thus, while the diagonal backbone is constant-curvature in this model, the rods themselves do not have constant curvature (unlike in conventional models), and computation of their length is thus more complicated.

As is commonly done in continuum robotics [1], we generate an inverse kinematics model between arc parameters (in this case the curvature, k) and actuation rod lengths. Thus, the input to our model is the desired backbone curvature k, and the output is the lengths of the two rods necessary to achieve the given curvature. Figure 3 shows a layout of the segment in the home configuration and defines all frames and geometric parameters.

O is the origin frame defined at the base of the segment. end is the end effector frame of the segment defined at the segment tip. A, B, C', and C are intermediate frames used to represent end, $\mathbf{p}_R$, and $\mathbf{p}_L$ in the O frame. $\mathbf{p}_R$ and $\mathbf{p}_L$ are points on the right and left actuation rods that are also constrained horizontal to C. θ is the angle of the backbone relative to the base, which remains constant even under bending. s is the distance along the centerline of the backbone from the base to an intermediary point as shown in Figure 3. Other segment dimensions are shown in 2.

To model the diagonal constant curvature transformation, the transformation matrix ${}^{O}\mathbf{T}_{end}$ is the product of transformations ${}^{O}\mathbf{T}_{A}$, ${}^{A}\mathbf{T}_{B}$, and ${}^{B}\mathbf{T}_{end}$. ${}^{O}\mathbf{T}_{A}$ is a translation from the origin to the base of the backbone, as well as a rotation to align the y-axis with the backbone tangent at A. ${}^{A}\mathbf{T}_{B}$ is a constant curvature transformation (as conventionally given in [1]) along the diagonal backbone from the base to the tip. ${}^{B}\mathbf{T}_{end}$ is a constant rotation to align axes with the end-effector frame and a translation to the middle of the end-effector. The relevant transformations are detailed below:

$$ {}^{O}\mathbf{T}_{A} = \begin{bmatrix} \mathbf{R}(\theta - \frac{\pi}{2}) & -\frac{w_b}{2} \\ 0 \quad 0 & 1 \end{bmatrix} \tag{1} $$

$$ {}^{A}\mathbf{T}_{B} = \begin{bmatrix} \mathbf{R}(kl_b) & -l_b \sin\left(\frac{kl_b}{2}\right) \operatorname{sinc}\left(\frac{kl_b}{2}\right) \\ 0 \quad 0 & l_b \operatorname{sinc}\left(kl_b\right) \\ & 1 \end{bmatrix} \tag{2} $$

$$ {}^{B}\mathbf{T}_{end} = \begin{bmatrix} \mathbf{R}(\frac{\pi}{2} - \theta) & 0 \\ 0 \quad 0 & 0 \\ & 1 \end{bmatrix} \begin{bmatrix} \mathbf{I} & -\frac{w_b}{2} \\ 0 \quad 0 & 0 \\ & 1 \end{bmatrix} \tag{3} $$

$$ {}^{O}\mathbf{T}_{end} = {}^{O}\mathbf{T}_{A}\,{}^{A}\mathbf{T}_{B}\,{}^{B}\mathbf{T}_{end} \tag{4} $$

where $\mathbf{R}()$ is the conventional 2D rotation matrix:

$$ \mathbf{R}(*) = \begin{bmatrix} \cos(*) & -\sin(*) \\ \sin(*) & \cos(*) \end{bmatrix} \tag{5} $$

and we have used an alternate form of the conventional constant curvature position

$$ \begin{bmatrix} \frac{1}{k}(1 - \cos ks) \\ \frac{1}{k} \sin ks \end{bmatrix} = \begin{bmatrix} s \sin \frac{ks}{2} \operatorname{sinc} \frac{ks}{2} \\ s \operatorname{sinc} ks \end{bmatrix} $$

by employing the half-angle identity and the sinc() function to eliminate the numerical singularity at $k = 0$, where

$$ \operatorname{sinc} x = \begin{cases} \frac{\sin x}{x}, & x \neq 0 \\ 1, & x = 0 \end{cases} \tag{6} $$

To facilitate calculation of actuation rod lengths, we also establish a transformation from the origin to frame C located a length s along the backbone. ${}^{O}\mathbf{T}_{A}$ remains unchanged from Equation (1). ${}^{A}\mathbf{T}_{C'}$ is a constant curvature transformation a distance s along the backbone, and ${}^{C'}\mathbf{T}_{C}$ is just a rotation by $-\theta$ so that frame C aligns with the global frame in the home configuration.

$$ {}^{A}\mathbf{T}_{C'} = \begin{bmatrix} \mathbf{R}(ks) & -s \sin\left(\frac{ks}{2}\right) \operatorname{sinc}\left(\frac{ks}{2}\right) \\ 0 \quad 0 & s \operatorname{sinc}\left(ks\right) \\ & 1 \end{bmatrix} \tag{7} $$

$$ {}^{C'}\mathbf{T}_{C} = \begin{bmatrix} \mathbf{R}(\frac{\pi}{2} - \theta) & 0 \\ 0 \quad 0 & 0 \\ & 1 \end{bmatrix} \tag{8} $$

$$ {}^{O}\mathbf{T}_{C} = {}^{O}\mathbf{T}_{A}\,{}^{A}\mathbf{T}_{C'}\,{}^{C'}\mathbf{T}_{C} \tag{9} $$

The position of a point on the actuation rods in the C frame are defined as ${}^{C}\mathbf{p}_{R}$ (right actuator) and ${}^{C}\mathbf{p}_{L}$ (left

IEEE Robotics and Automation Letters (RA-L) paper, presented at ICRA 2026, Vienna, Austria. Cite as RA-L paper.

actuator) according to the design variables as follows (in 2D homogeneous point form):

$$^{C}\mathbf{p}_R = \begin{bmatrix} \frac{w_b+w_t}{2} - s\cos(\theta) & 0 & 1 \end{bmatrix}^\top \tag{10}$$

$$^{C}\mathbf{p}_L = \begin{bmatrix} \frac{w_b-w_t}{2} - s\cos(\theta) & 0 & 1 \end{bmatrix}^\top \tag{11}$$

These two points are then represented in the global frame as

$$\mathbf{p}_R = {}^{O}\mathbf{T}_C(s)\,{}^{C}\mathbf{p}_R(s) \tag{12}$$

$$\mathbf{p}_L = {}^{O}\mathbf{T}_C(s)\,{}^{C}\mathbf{p}_L(s) \tag{13}$$

With the equation for the actuation rods defined, an arc length integral can be used to determine the length of the actuation rods. The arc length integral will integrate the magnitude of the derivative of the actuation rod line functions ($\mathbf{p}_{R,O}$,$\mathbf{p}_{L,O}$) with respect to the distance along the backbone (s) over the length of the backbone (0 to l_b). Define the length of the right actuation rod as l_r and the length of the left actuation rod as l_l.

$$l_R = \int_0^{l_b} \left\| \frac{d}{ds}(\mathbf{p}_R) \right\| ds \tag{14}$$

$$l_L = \int_0^{l_b} \left\| \frac{d}{ds}(\mathbf{p}_L) \right\| ds \tag{15}$$

where the norm is applied only to the position part, not including the 1 element that is part of the homogeneous form. We evaluate these integrals numerically by sampling the $\mathbf{p}_R$ and $\mathbf{p}_L$ curves at discrete values of s between 0 and l_b and summing up the discrete lengths. Note that in contrast to conventional constant curvature models, the rod paths are not circular arcs even though the backbone follows a circular arc. It turns out that under the constant curvature assumption, the actuator lengths are equidistant from l_0 (as intuited by symmetry), and thus it is sufficient to calculate only l_L or l_R. If forward kinematics is desired, we use a numerical root finding algorithm to determine the curvature k associated with a particular set of lengths l_R and l_L equidistant from l_0.

A. Assumptions for Model Validity

The constant curvature model in this section is valid when:

- The actuation rods are displaced equal amounts in opposite directions away from the straight home configuration.
- The manipulator is operated at curvatures within the elastic strain limits of the backbone material. That is, $|k| < \frac{2\epsilon_{max}}{t}$, where ϵ_{max} is the material's elastic strain limit and t is the thickness of the backbone wall.
- The curvature is less than the geometric limit that would result in self intersection of the material. In the constant-curvature case, this limit can be well approximated as $|k| < \frac{1}{w_b}$
- The manipulator is not subject to extremely large loads. However, even large loads can be handled without loss of the constant curvature validity because of the high output stiffness afforded by diagonlizing the backbone, as we show experimentally in Section V.

B. Conventional Constant Curvature Model

In the Section V, we will compare our diagonal backbone constant curvature model to the conventional constant curvature model for straight backbones (parallel to actuation rods). This conventional model is simply given by the constant curvature transformation itself, without the pre- and post- transformations that account for the diagonality of the backbone. Thus, the transformation from O to the end-effector in a conventional constant curvature model is

$${}^{O}\mathbf{T}_{end,CC} = \begin{bmatrix} \mathbf{R}(kL_b) & \begin{matrix} -L_b \sin\left(\frac{kL_b}{2}\right)\operatorname{sinc}\left(\frac{kL_b}{2}\right) \\ L_b \operatorname{sinc}\left(kL_b\right) \end{matrix} \\ \begin{matrix} 0 & 0 \end{matrix} & 1 \end{bmatrix} \tag{16}$$

IV. Modeling: 2-DOF, Variable Curvature

The following section generalizes the previous model to accommodate any general 2-DOF actuation (l_L and l_R are no longer assumed to be equidistant from l_0), and allow for variable curvature along the length. We parameterize the curvature along the backbone with n discrete constant curvature segments, each having a potentially different curvature k_i. Thus, a transformation along the centerline of the backbone can be modeled as the product of constant curvature transformations. Equation (17) below gives the transformation along the entire backbone from A to B, while (18) describes the transformation from A to an intermediate segment end point C_i, where $0 \leq i \leq n$:

$${}^{A}\mathbf{T}_B = {}^{0}\mathbf{T}_1\,{}^{1}\mathbf{T}_2\,{}^{2}\mathbf{T}_3 ...\,{}^{n-1}\mathbf{T}_n \tag{17}$$

$${}^{A}\mathbf{T}_{C_i} = {}^{0}\mathbf{T}_1\,{}^{1}\mathbf{T}_2\,{}^{2}\mathbf{T}_3 ...\,{}^{i-1}\mathbf{T}_i \tag{18}$$

where the intermediate discrete curvature transformations above are

$${}^{i-1}\mathbf{T}_i = \begin{bmatrix} \mathbf{R}(k_i\Delta s_i)) & \begin{matrix} -\Delta s_i \sin\left(\frac{k_i\Delta s_i}{2}\right)\operatorname{sinc}\left(\frac{k_i\Delta s_i}{2}\right) \\ \Delta s_i \operatorname{sinc}\left(k_i\Delta s_i\right) \end{matrix} \\ \begin{matrix} 0 & 0 \end{matrix} & 1 \end{bmatrix} \tag{19}$$

with $\Delta s_i = s_i - s_{i-1}$. To determine the set of discrete curvatures $\mathbf{k} = \{k_1, k_2, ..., k_n\}$ for a given actuation, we minimize the elastic energy subject to rod length constraints, that is, we solve a constrained energy minimization problem of the form:

$$\underset{\mathbf{k}}{\operatorname{argmin}} \;\; u = \frac{1}{2}\sum_{i=1}^{n} EIk_i^2 \tag{20}$$

where EI is the bending rigidity, subject to constraints:

$$l_R = \int_0^{l_b} \left\| \frac{d}{ds}(\mathbf{p}_R) \right\| ds \approx \sum_{i=0}^{n-1} \|\mathbf{p}_{R,i+1} - \mathbf{p}_{R,i}\| \tag{21}$$

$$l_L = \int_0^{l_b} \left\| \frac{d}{ds}(\mathbf{p}_L) \right\| ds \approx \sum_{i=0}^{n-1} \|\mathbf{p}_{L,i+1} - \mathbf{p}_{L,i}\| \tag{22}$$

where

$$\mathbf{p}_{R,i} = {}^{O}\mathbf{T}_{C_i} \begin{bmatrix} \frac{w_b+w_t}{2} - s_i\cos(\theta) & 0 & 1 \end{bmatrix}^\top \tag{23}$$

$$\mathbf{p}_{L,i} = {}^{O}\mathbf{T}_{C_i} \begin{bmatrix} \frac{w_b-w_t}{2} - s_i\cos(\theta) & 0 & 1 \end{bmatrix}^\top \tag{24}$$

IEEE Robotics and Automation Letters (RA-L) paper, presented at ICRA 2026, Vienna, Austria. Cite as RA-L paper.

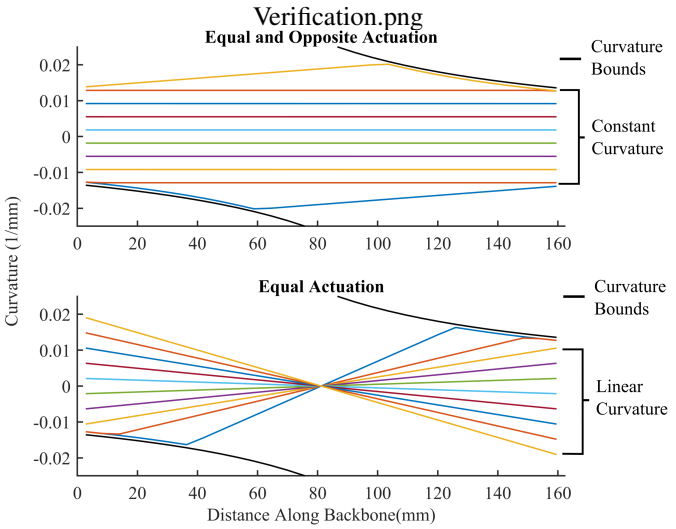

Fig. 4: Both plots show the curvature along the backbone. The black lines indicate the upper and lower curvature bounds. Each colored line describes the curvature along the backbone for a given actuation input. The top graph shows instances of equal and opposite actuation (up to ±90 mm). These cases result in constant curvature until the curvature bounds are reached, verifying the consistency of the constant curvature model with the general one and validating the constant curvature assumption. The bottom graph shows instances of equal actuation (up to ±40 mm). These result in linear curvature until the curvature bounds are reached.

and also subject to location-dependent bounds on the curvatures to disallow curvatures that in self intersection of the material:

$$\frac{-1}{w_b - \frac{1}{2}(s_i + s_{i+1})\cos(\theta)} \leq k_i \leq \frac{1}{\frac{1}{2}(s_i + s_{i+1})\cos(\theta)} \quad (25)$$

These bounds are a linear approximation based on the undeformed manipulator geometry. Avoiding self-intersection in a general deformed state is a complex problem that we leave to future work. This constrained optimization problem with upper and lower bounds and nonlinear constraints can be solved by standard routines optimization software packages. For example, we use Matlab's fmincon() with rod length nonlinear equality constraints and bounds on the curvatures.

A. Curvature Profiles

We can use the general curvature model to further verify the constant curvature assumption and gain intuition about curvature profiles in general. Figure 4 (top) shows the resulting curvature profiles produced by the general model when the actuators are displaced equal amounts in opposite directions, as shown in the top row of Figure 5. This verifies that the constant curvature assumption is valid in this case, when the geometric curvature limit is not exceeded. Figure 4 (bottom) shows that equal actuator displacement in the same direction produces linearly varying curvature, as shown in the bottom row of Figure 5, until the curvature limits are reached. This is also an intuitive result which leads to diagonal translation of the end-effector without rotation. Videos of both motion profiles can be found in the video attachment.

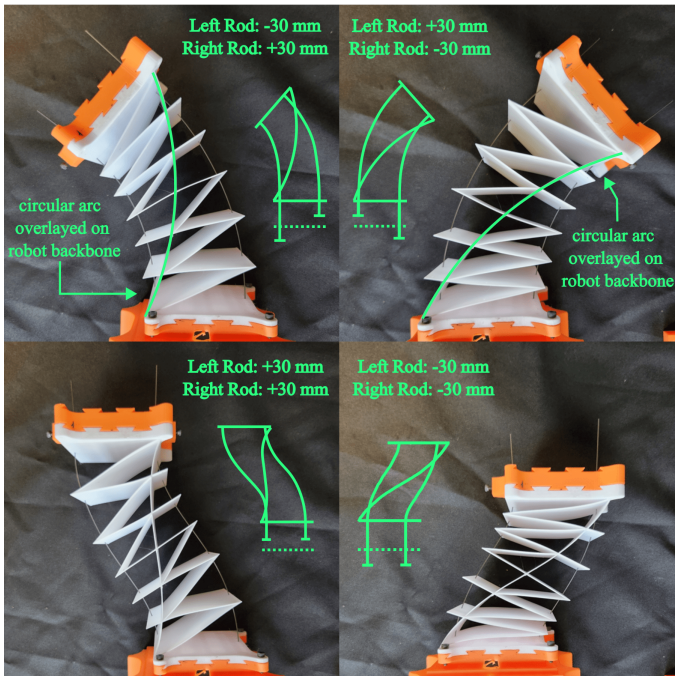

Fig. 5: The top left image shows the robot under constant curvature with the left rod contracted 30 mm and the right rod extended 30 mm. The top right image shows constant curvature in the other direction with the actuations reversed. The bottom left image shows the robot with both rods extended 30 mm. The tip orientation of the robot remains the same as it does in home configuration. The same is shown in the bottom right image with the rods instead retracted.

V. Experimental Validation

We performed several experiments to validate the kinematic models presented in the previous sections, confirm the ability of the proposed bending segment design to exhibit a controllable 2-DOF workspace and extremely high output stiffness.

A. Constant Curvature Kinematic Validation and Workspace

The robot, detailed in Section II, was assembled and actuated around its workspace. Points were sampled by commanding specific actuation rod lengths, and the tip position was measured experimentally using a graph paper background and manually recorded points at a reference location on the robot. These points were compared against the model predicted positions calculated in MATLAB using the kinematic models. To account for reference frame alignment with our coordinate measurement system, we rigidly registered the experimental dataset to the model dataset before calculating error.

We first assessed the accuracy of the diagonal constant curvature model of Section III by commanding actuation rod displacements in equal and opposite directions. The range of actuation lengths was -45 mm to 45 mm in 5 mm increments. Figure 6 (top graph) compares the model-predicted (blue circles) tip position to the experimentally measured tip position (black dots) across the constant-curvature configuration space. Our model (constant curvature along the diagonal backbone) had an average error of 0.8 mm and maximum error of 2.2 mm at the edge of the workspace. These small errors are likely due to human error in taking the measurements, manufacturing

IEEE Robotics and Automation Letters (RA-L) paper, presented at ICRA 2026, Vienna, Austria. Cite as RA-L paper.

Curvature Validation.png

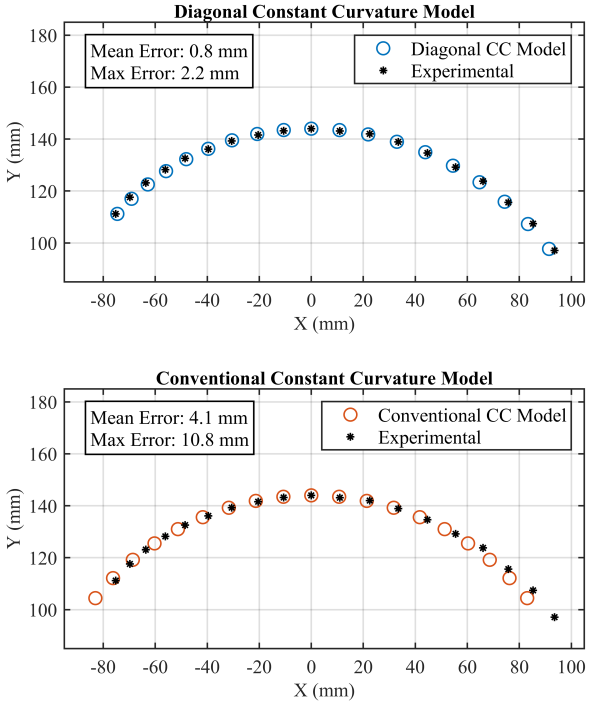

Fig. 6: This figure shows the tip position of the single segment robot under a series of different equal and opposite rod actuations, compared to two models. Top: our diagonal constant curvature model. Bottom: the conventional constant curvature model.

discrepancies, and friction between the actuation rods and their guide holes. In contrast, the conventional constant curvature model (Section III-B) exhibits a mean error of 4.1mm and maximum error of 10.8mm. This experiment further validates that the diagonal backbone indeed bends in a constant curvature shape when the actuators are displaced equal amounts in opposite directions, and that the structure of our new model is correct. Note, in particular that the asymmetry of the workspace (due to the asymmetry of the backbone) is captured by our model due to its pre- and post- transformations applied to the constant curvature mapping, while the conventional constant-curvature model expects a symmetric workspace.

B. Variable Curvature Kinematic Validation and Workspace

We next assessed the accuracy of the more general variable curvature model of Section IV by commanding a set of actuation rod displacements spanning the range of the configuration space (25 points generated from every combination of actuations: -30mm to 30mm in 15mm increments). Experimental data was collected in the same manner as the constant curvature model validation. In the model, 9 discrete constant-curvature segments were used. Figure 7 compares the model prediction to experiment across all these actuator combinations. The variable curvature model exhibited had a mean error of 0.4mm and maximum error of 1.7mm. This agreement validates the more general modeling approach, and the experiments confirm the ability of the diagonal backbone bending segment to be controlled in a significant 2-

Curvature Model And Workspace.png

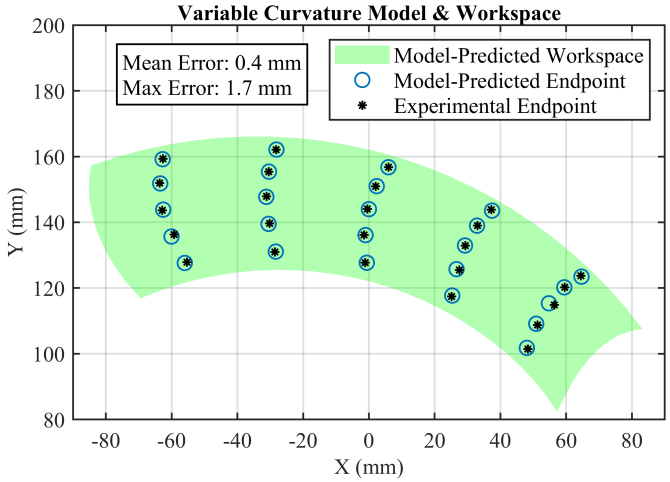

Fig. 7: This figure shows the tip position of the single segment robot under a series of general rod actuations up to 30mm. The model-predicted points (blue circles) are plotted against the experimental points (black asterisks). The green background shows the workspace for the robot under theoretical actuation up to 40mm.

DOF planar configuration space, unlike conventional constant-curvature bending segment designs which only exhibit a single controllable DOF if the backbone is inextensible [1].

Using our general model, the workspace of a single 2-DOF bending segment is depicted in Figure 7 (green area) when the rods are actuated within a range of up to $\pm$ 40mm from the starting length. While the rods can be pushed and pulled beyond this range, doing so requires greater backbone curvature and force and causes internal collisions between the fins. Unlike conventional straight backbone continuum robots, the workspace is asymmetric, and the robot can translate diagonally while maintaining a constant angle as shown in Figure 5.

C. Output Stiffness Validation and Comparison

Another main advantage of the diagonal backbone segment over a straight backbone segment is that we do not observe the S-shape mode of deformation (second harmonic mode) in the diagonal backbone design, under loads which cause large S-shaped deflections in straight backbone designs. This allows the segment to bear greater loads without deformation than equivalent straight backbone designs. To demonstrate this, two bending segments (one with conventional parallel backbone and one with diagonal backbone) were placed into a cantilevered position and loaded with weights hung from the tip up to 900g while the rod actuators were held fixed. The two segments are have the same size (75x75x144mm), thickness (0.8mm), material (PETG), and similar fin structures increasing torsional rigidity and rigidity about one bending axis. The comparison focuses on the resulting output stiffness while the rod lengths are locked. Figure 8 demonstrates the results, showing the quantitative deflection as measured by a motion capture system (OptiTrack) and several pictures of the robot's shape. The conventional backbone design exhibits significant s-shape deflection under only self-weight, and the

IEEE Robotics and Automation Letters (RA-L) paper, presented at ICRA 2026, Vienna, Austria. Cite as RA-L paper.

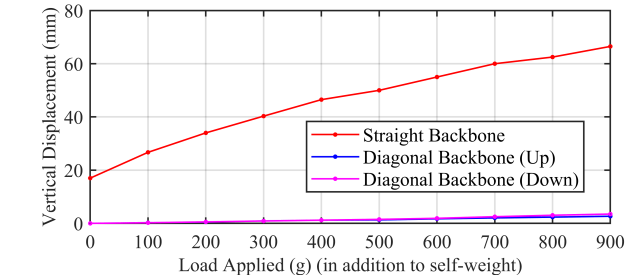

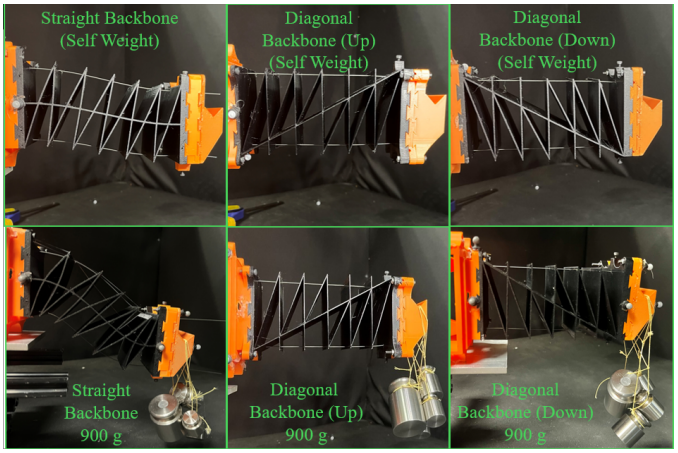

Fig. 8: **Top**: Displacement is plotted vs. external load applied in our cantilevered load experiments. The straight backone design deflects much more, and the diagonal backbone design almost eliminates tip deflection. **Bottom**: Snapshots of the experiments are shown in the six labeled panels. The s-shaped mode of deformation can be clearly seen in the straight backbone design, even under self-weight only, while the diagonal backbone design exhibits minimal deflection in both diagonal up and diagonal down configurations.

deflection grows increasingly large as the tip load is applied. In contrast, the diagonal backbone design exhibits minimal deflection throughout the experiment in both diagonal up and diagonal down configurations.

The straight backbone segment exhibited significant deformation with no load applied (only self weight), and with the 900g weight, it deformed even more into the expected S-shape. On the other hand, the diagonal backbone segment showed minimal deformation both with and without the 900g weight as shown in Figure 8, and did not exhibit an s-shape passive bending mode. This experiment shows the that the diagonal backbone significantly increases output stiffness by eliminating the S-shape mode of deformation.

D. Two Segment Robot Demonstration

To further demonstrate the potential of diagonal backbone bending segments, a two-segment, 4-DOF robot was built where the segments were offset 90° from each other as shown in Figure 2. We implemented open-loop control of the four actuators to each follow a different triangle wave profile of displacement over time, such that the tip follows a complex 3D tip trajectory. We ran this open-loop trajectory control program on the two segment robot, both in free space and with a 200g weight added to the end effector, and tracked its tip motion with an Optitrack IR camera system. The video

(weight) 2.png

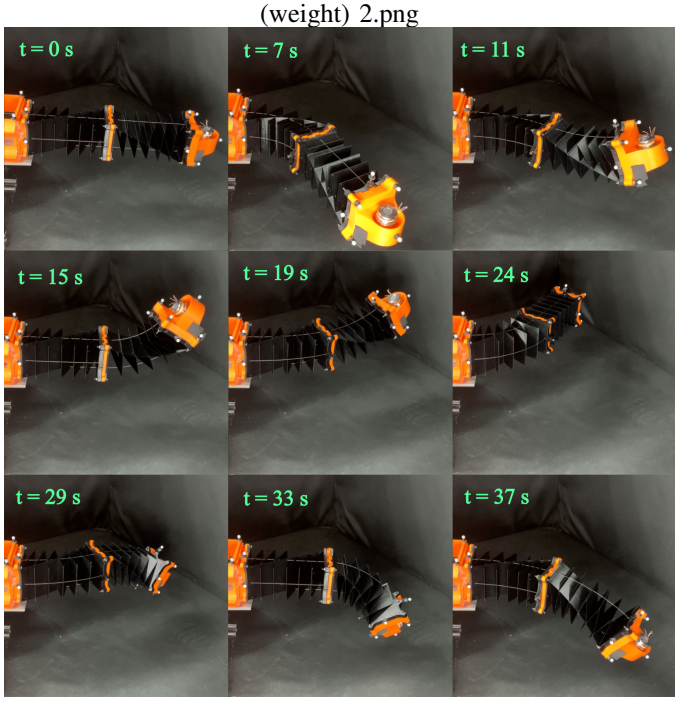

Fig. 9: The images show the 2-segment robot following a specified 3D path around its workspace with a 200g weight attached to the robot end-effector.

vs Model trajectories.jpg

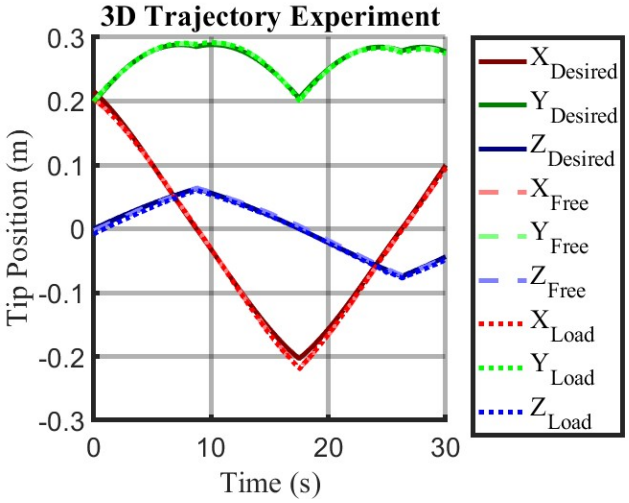

Fig. 10: This figure shows the coordinates of the 3D tip trajectories of the experimental robot overlaid on top of the desired model-predicted trajectory (Desired). Trajectories are shown for the robot operating in free space (Free) and with a 200g tip load attached (Load) compared to a desired trajectory given by our model.

attachment to this paper shows the resulting robot motion, and still pictures at points in time can be seen in Figure 9. Figure 10 shows the resulting 3D cartesian tip trajectories for the loaded and unloaded cases, overlaid on each other and on the desired trajectory. The error remains under 20mm for the entire trajectory, regardless of the added weight, and there is no evidence of vibration despite the trajectory containing abrupt changes in actuator and tip velocity.

IEEE Robotics and Automation Letters (RA-L) paper, presented at ICRA 2026, Vienna, Austria. Cite as RA-L paper.

VI. Conclusion

We developed a model and experimentally validated a prototype for a diagonal backbone continuum robot. The robot demonstrates impressive capabilities for continuum robots, dramatically increasing output stiffness (see Figure 8) with a large range of motion (see Figure 8). These properties come from the diagonal backbone design constraining the s-shape mode of deformation that typically weakens continuum robot output stiffness. Two kinematic models for the robot were presented. By actuating the rods equal distances in opposite directions, the backbone follows a constant curvature shape, allowing for simple 1-DOF control using a modified conventional constant model. For any actuation of the rods (2-DOF control), the robot can be modeled by discretizing the backbone into multiple constant curvature segments, solved by strain energy minimization. Diagonal backbone segments can improve continuum robots by enabling them to manipulate larger loads while minimizing unwanted deformation. This could enable new capabilities in applications with relatively high precision and strength requirements (robotic surgery), requirements to move heavy loads with a lightweight manipulator (space applications), and requirements to minimize passive vibration (high bandwidth gaits for locomoiton). In future work, we would like to see higher-DOF robots combining multiple segments at different angles, and application of the concept at smaller scales for surgical tools.

References

[1] R. J. Webster, III and B. A. Jones, "Design and Kinematic Modeling of Constant Curvature Continuum Robots: A Review," *The International Journal of Robotics Research*, vol. 29, no. 13, pp. 1661–1683, 2010.

[2] J. Burgner-Kahrs, D. C. Rucker, and H. Choset, "Continuum Robots for Medical Applications: A Survey," *IEEE Transactions on Robotics*, vol. 31, no. 6, pp. 1261–1280, Dec. 2015.

[3] K. Wu, G. Zhu, L. Wu, W. Gao, S. Song, C. M. Lim, and H. Ren, "Safety-enhanced model-free visual servoing for continuum tubular robots through singularity avoidance in confined environments," *IEEE Access*, vol. 7, pp. 21 539–21 558, 2019.

[4] K. Li, Z. Qi, and X. Feng, "A review of continuum robots for surgical applications," *Applied and Computational Engineering*, 2023.

[5] I. D. Walker and C. University, "Use of continuum robots for remote inspection operations," in *2017 Computing Conference*, 2017, pp. 1382–1385.

[6] I. Good, S. Balaji, D. Oh, S. Thomas, and J. I. Lipton, "Torque responsive metamaterials enable high payload soft robot arms," *ArXiv*, vol. abs/2501.09819, 2025.

[7] C. Liu, L. Dong, Z. Chen, R. Zhang, M. Tian, and X. Wang, "Kinematic modeling and control of a continuum robot in confined spaces," in *2024 30th International Conference on Mechatronics and Machine Vision in Practice (M2VIP)*, 2024, pp. 1–6.

[8] F. Stella and J. Hughes, "The science of soft robot design: A review of motivations, methods and enabling technologies," *Frontiers in Robotics and AI*, vol. Volume 9 - 2022, 2023.

[9] C. Abah, A. L. Orekhov, G. L. H. Johnston, and N. Simaan, "A multi-modal sensor array for humanrobot interaction and confined spaces exploration using continuum robots," *IEEE Sensors Journal*, vol. 22, no. 4, pp. 3585–3594, 2022.

[10] X. Wang, Q. Lu, D. Lee, Z. Gan, and N. Rojas, "A soft continuum robot with self-controllable variable curvature," *IEEE Robotics and Automation Letters*, vol. 9, no. 3, pp. 2016–2023, 2024.

[11] N. G. Cheng, M. B. Lobovsky, S. J. Keating, A. M. Setapen, K. I. Gero, A. E. Hosoi, and K. D. Iagnemma, "Design and Analysis of a Robust, Low-cost, Highly Articulated manipulator enabled by jamming of granular media," in *2012 IEEE International Conference on Robotics and Automation*. IEEE, may 2012, pp. 4328–4333.

[12] Y.-J. Kim, S. Cheng, S. Kim, and K. Iagnemma, "A Novel Layer Jamming Mechanism With Tunable Stiffness Capability for Minimally Invasive Surgery," *IEEE Transactions on Robotics*, vol. 29, no. 4, pp. 1031–1042, aug 2013.

[13] A. Jiang, G. Xynogalas, P. Dasgupta, K. Althoefer, and T. Nanayakkara, "Design of a variable stiffness flexible manipulator with composite granular jamming and membrane coupling," in *2012 IEEE/RSJ International Conference on Intelligent Robots and Systems*. IEEE, oct 2012, pp. 2922–2927.

[14] D. Bruder, M. A. Graule, C. B. Teeple, and R. J. Wood, "Increasing the payload capacity of soft robot arms by localized stiffening," *Science Robotics*, vol. 8, no. 81, p. eadf9001, 2023.

[15] L. Yang, Z. Zhang, Z. Zhang, Y. Lou, S. Han, J. Liu, L. Fang, and S. Zhang, "Design of heavy-load soft robots based on a dual biomimetic structure," *Biomimetics*, vol. 9, no. 7, 2024.

[16] M. Roshanfar, A. Sayadi, J. Dargahi, and A. Hooshiar, "Stiffness adaptation of a hybrid soft surgical robot for improved safety in interventional surgery," in *2022 44th Annual International Conference of the IEEE Engineering in Medicine & Biology Society (EMBC)*, 2022, pp. 4853–4859.

[17] P. Rao, C. Pogue, Q. Peyron, E. Diller, and J. Burgner-Kahrs, "Modeling and analysis of tendon-driven continuum robots for rod-based locking," *IEEE Robotics and Automation Letters*, vol. 8, no. 6, pp. 3126–3133, 2023.

[18] Y. Sun and T. C. Lueth, "Enhancing torsional stiffness of continuum robots using 3-d topology optimized flexure joints," *IEEE/ASME Transactions on Mechatronics*, vol. 28, no. 4, pp. 1844–1852, 2023.

[19] C. Chen, H. Zhang, P. Yan, H. Huang, and B. Li, "A seahorse-inspired continuum robot with high load capacity," *IEEE Robotics and Automation Letters*, vol. 9, no. 2, pp. 1835–1842, 2024.

[20] Y. Li, H. Huang, and B. Li, "Design of a deployable continuum robot using elastic kirigami-origami," *IEEE Robotics and Automation Letters*, vol. 8, no. 12, pp. 8382–8389, 2023.

[21] J. Santoso and C. D. Onal, "An origami continuum robot capable of precise motion through torsionally stiff body and smooth inverse kinematics," *Soft Robot.*, vol. 8, no. 4, pp. 371–386, Aug. 2021.

[22] J. A. Childs and C. Rucker, "Leveraging geometry to enable high-strength continuum robots," *Frontiers in Robotics and AI*, vol. Volume 8 - 2021, 2021.

[23] Q. Ze, S. Wu, J. Nishikawa, J. Dai, Y. Sun, S. Leanza, C. Zemelka, L. S. Novelino, G. H. Paulino, and R. R. Zhao, "Soft robotic origami crawler," *Science Advances*, vol. 8, no. 13, p. eabm7834, 2022.

[24] Y. Sun, Y. Lv, S. Xie, Q. Guo, L. Wang, and L. Yang, "Kresling origami with differentiation flaw design for multidirectional crawling robot," *IEEE Robotics and Automation Letters*, vol. 9, no. 9, pp. 7707–7714, 2024.

[25] Y.-J. Kim, S. Cheng, S. Kim, and K. Iagnemma, "A Stiffness-Adjustable Hyperredundant Manipulator Using a Variable Neutral-Line Mechanism for Minimally Invasive Surgery," *IEEE Transactions on Robotics*, vol. 30, no. 2, pp. 382–395, apr 2014.

[26] K. Butler, A. Orekhov, J. Childs, and D. C. Rucker, "A Rigid Mechanism with Uniform, Variable Curvature," *ASME Journal of Medical Devices*, 2016.

[27] Y. Wang, K. Yang, and H. Jin, "Design of a hyper-redundant manipulator with zigzag mechanism doublet," *IEEE Robotics and Automation Letters*, vol. 10, no. 3, pp. 2990–2997, 2025.

[28] K. Oliver-Butler, J. Till, and C. Rucker, "Continuum robot stiffness under external loads and prescribed tendon displacements," *IEEE Transactions on Robotics*, vol. 35, no. 2, pp. 403–419, 2019.

[29] J. Rommers, V. van der Wijk, and J. L. Herder, "A new type of spherical flexure joint based on tetrahedron elements," *Precision Engineering*, vol. 71, pp. 130–140, 2021.